Particles II

Access the latest eBook →

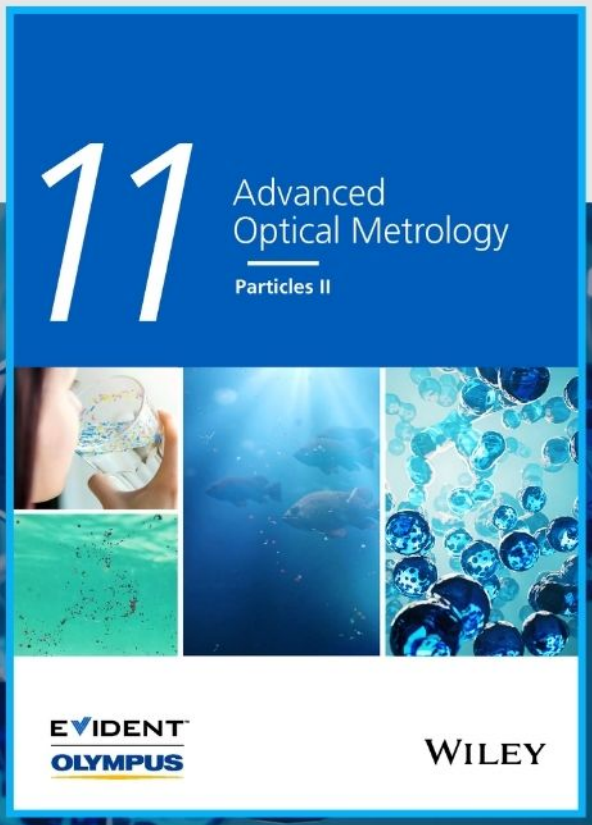

Impact on Biological Systems and the Environment

This eBook is dedicated to the research of Professor David Wertheim.
In collaboration with various groups, Professor Wertheim uses confocal microscopy to analyse the impact of different types of particles on human health and the environment, with a focus on human health-hazardous particles detected with solid-state nuclear track detectors (SSNTD). Download for free, today.

EVIDENT
OLYMPUS

WILEY

ADVANCED FUNCTIONAL MATERIALS
www.afm-journal.de

Revealing 2D Magnetism in a Bulk CrSBr Single Crystal by Electron Spin Resonance

Fabrizio Moro, Shenggang Ke, Andrés Granados del Águila, Aljoscha Söll, Zdenek Sofer, Qiong Wu, Ming Yue, Liang Li, Xue Liu, and Marco Fanciulli*

2D magnets represent material systems in which magnetic order and topological phase transitions can be observed. Based on these phenomena, novel types of computing architectures and magnetoelectronic devices can be envisaged. Unlike conventional magnetic films, their magnetism is independent of the substrate and interface qualities, and 2D magnetic properties manifest even in formally bulk single crystals. However, 2D magnetism in layered materials is rarely reported often due to weak exchange interactions and magnetic anisotropy, and low magnetic transition temperatures. Here, the electron spin resonance (ESR) properties of a layered antiferromagnetic CrSBr single crystal are reported. The *W*-like shape angular dependence of the ESR linewidth provides a signature for room temperature spin–spin correlations and for the XY spin model. By approaching the Néel temperature the arising of competing intralayer ferromagnetic and interlayer antiferromagnetic interactions might lead to the formation of vortex and antivortex pairs. This argument is inferred by modeling the temperature dependence of the ESR linewidth with the topological Berezinskii-Kosterlitz-Thouless phase transition. These findings together with the chemical stability and semiconducting properties, make CrSBr a promising layered magnet for future magneto- and topological-electronics.

1. Introduction

2D magnets are recently gaining interest from the scientific community because they offer the possibility to be easily exfoliated down to few layer and even to the monolayer limit while retaining magnetic order.[1] Their magnetic properties are characterized by strong intralayer exchange magnetic interactions and weak dipolar or exchange interlayer magnetic interactions. Unlike ultrathin magnetic films, their magnetism is independent of the substrate and interface qualities, and their 2D magnetic properties are apparent even in formally bulk (3D) materials. Therefore, they can be incorporated into heterostructures[2] to make new multifunctional devices with combined electric, optical and magnetic properties for applications in spintronics, magnetoelectronics, quantum computing, and magneto-optical devices.

The interest around these materials has sparked since the recent discovery

F. Moro, M. Fanciulli
Department of Materials Science
University of Milano-Bicocca
via R. Cozzi 55, Milano 20125, Italy
E-mail: fabrizio.moro@unimib.it

S. Ke, L. Li, X. Liu
Information Materials and Intelligent Sensing Laboratory of Anhui Province
Institutes of Physical Science and Information Technology
Anhui University
Hefei 230601, China

A. G. del Águila
Institute for Functional Intelligent Materials
National University of Singapore
Singapore 117544, Singapore

The ORCID identification number(s) for the author(s) of this article can be found under https://doi.org/10.1002/adfm.202207044.

DOI: 10.1002/adfm.202207044

A. Söll, Z. Sofer
Department of Inorganic Chemistry
Faculty of Chemical Technology
University of Chemistry and Technology Prague
Technicka 5, Prague 6 166 28, Czech Republic

Q. Wu, M. Yue
Faculty of Materials and Manufacturing
Key Laboratory of Advanced Functional Materials
Ministry of Education of China
Beijing University of Technology
Beijing 100124, China

L. Li
Key Laboratory of Materials Physics
Anhui Key Laboratory of Nanomaterials and Nanotechnology
Institute of Solid State Physics
Hefei Institutes of Physical Science
Chinese Academy of Sciences
Hefei 230031, China

of long-range ferromagnetic (FM) order in $Cr_2Ge_2Te_6$[3] and CrI_3[4] VdW magnets. According to the Mermin–Wagner (MW) theorem "at, any nonzero temperature, a 1-D or 2-D isotropic spin-Heisenberg model with finite-range exchange interaction can be neither ferromagnetic nor antiferromagnetic."[5] In other words, long-range order in 2D magnets is strongly suppressed in isotropic spin systems with short-range interactions at finite temperature due to thermal fluctuations. Thus, magnetic order in Heisenberg 2D magnets can exist only at $T = 0$ K. However, magnetic anisotropy due to spin–orbit coupling and/or dipolar interactions opens a gap in the magnon excitations at low-momentum ($q \approx 0$), thus lifting the MW theorem and leading to the observation of magnetic order at finite temperature. Furthermore, 2D magnets represent a model system for the observation of new quantum phenomena and phase transitions such as skyrmions and topological phase transitions with the formation of vortex and antivortex pairs described by the Berezinskii–Kosterlitz–Thouless (BKT) model for which Kosterlitz and Thouless won the Nobel prize in 2016.[6] Therefore, 2D magnets hold the potential to discover new quantum phenomena at nanoscale or to engineer materials with functionalities based on novel quantum degrees of freedom.

Nowadays, many Van der Waals (VdW) magnets with both antiferromagnetic and ferromagnetic properties have been discovered and many have been theoretically predicted to possess magnetic order temperature above room temperature. However, there are many drawbacks that hinder their practical applications such as low Curie temperatures, extreme air instabilities, and poor transport properties.[7] Thus, the understanding of the magnetic properties of such materials is of fundamental importance for the realization of devices in spintronics and magnetoelectronics with tailored properties and optimized performances.

Within the family of 2D magnets, CrSBr antiferromagnetic semiconductor has recently attracted particular interest because of its relatively high antiferromagnetic ($T_N \approx 132$ K) and ferromagnetic ($T_C \approx 180$ K) ordering temperatures and chemical stability.[8] In addition, large negative magnetoresistance and semiconducting transport properties, stability under ambient conditions, and gate-tunable magnetic ordering have been found.[2,7a,9] Bulk CrSBr crystallizes in an orthorhombic structure, in which each Cr ion is coordinated by four chalcogenide and two halide ions in a distorted octahedron. The robust 2D ferromagnetism of the CrSBr is ascribed to the halogen-mediated (Cr–Br–Cr) and chalcogen-mediated (Cr–S–Cr) strong superexchange interactions, $J_1 = 1.74$ and $J_2 = 0.86$ meV, respectively and weak interlayer coupling J', namely $J / J' \approx 10^3 - 10^4$.[10] Monte Carlo calculations predict that monolayers of CrSBr have a ferromagnetic ordering temperature $T_C \approx 290$ K.[2]

Electron spin resonance (ESR) is a powerful tool for the study of technologically relevant static and dynamic magnetic properties such as magnetic anisotropies, magnetic transition temperatures, spin relaxation phenomena, spin–spin correlations, and spin dimensionalities. Notably, the ESR technique has been recently used as a method to investigate the BKT transition in 2D magnets.[11] Examples of VdW magnetic semiconductors studied by ESR are $CrBr_3$,[11a] K_2MnF_4,[12] $CrCl_3$,[13] $CrSbSe_3$[14] and $Cr_2Ge_2Te_6$.[15]

Here we report on a comprehensive ESR study on a bulk CrSBr single crystal as function of the crystal rotation relative to the external applied magnetic field and temperature, and obtain insights on the magnetic anisotropy properties, spin–spin correlations, magnetic phase transitions, spin dimensionality and infer on the possibility to observe the topological BKT phase transition.

2. Results and Discussion

2.1. Structural Studies

The centimeter-size bulk CrSBr crystals were synthesized by using a chemical vapor transport method (see Experimental Section). As reported in **Figure 1**a, the CrSBr shows a layered crystal structure with Van der Waals interactions formed between each Br-CrS-Br sandwiched layer along the *c*-axis. Our high-resolution transmission electron microscopy (TEM) studies with the view direction along the *c*-axis indicate the high crystal quality. Notably, the TEM samples with a thickness <20 nm (Figure 1b) were prepared in ambient environment (see Experimental Section), and stored in air for more than two weeks before conducting TEM measurements. The well-matched crystal structure with our simulation (Figure 1d) and clear edge of the crystal indicate highly preserved crystallinity even down to thin-film and air-stable property of this material. From TEM studies we determine the lattice parameters with 1.77 and 2.28 Å along the *a* and *b*-axis, respectively. The high quality of the synthesized CrSBr crystal can also be confirmed by our Raman spectroscopy studies. Figure 1e shows the contour map of polarization-dependent Raman peak intensity under linear polarized laser excitations at 2.33 eV. From our observations, these three Raman modes can be attributed to A_g modes with out-of-plane vibration configurations. The A_g^1 (114.6 cm^{-1}) and A_g^3 (344.1 cm^{-1}) modes reach maximum intensity when the linear excitation is along the *b* axis, while the A_g^2 (245.4 cm^{-1}) mode shows maximum intensity when the laser is along the *a* axis. These results are consistent with a recent study suggesting the existence of quasi-1D electron-phonon coupling in CrSBr crystals.[16] XPS, SEM, and EDS studies confirm that CrSBr is a single crystal, with stoichiometric ratio of Cr:S:Br (Figures S1 and S2, Supporting Information).

2.2. ESR Angular Dependence

In the following the results of the angular and temperature electron spin resonance measurements on a CrSBr single crystal are presented. The crystal is rotated with rotation angles θ_H and φ_H, in the out-of-plane and in-plane configurations, that is by rotating the crystal around the [100] and [001] axes (i.e., *a* and *c* respectively) with respect to the applied magnetic field H, respectively (**Scheme 1**b). Scheme 1c reports the ESR phenomenon with the precession of the magnetization vector M around the applied magnetic field H. The angular-dependent ESR contour plots measured for the out-of-plane and in-plane configurations are shown in **Figure 2** along with the spectra recorded in correspondence with the turning points of the

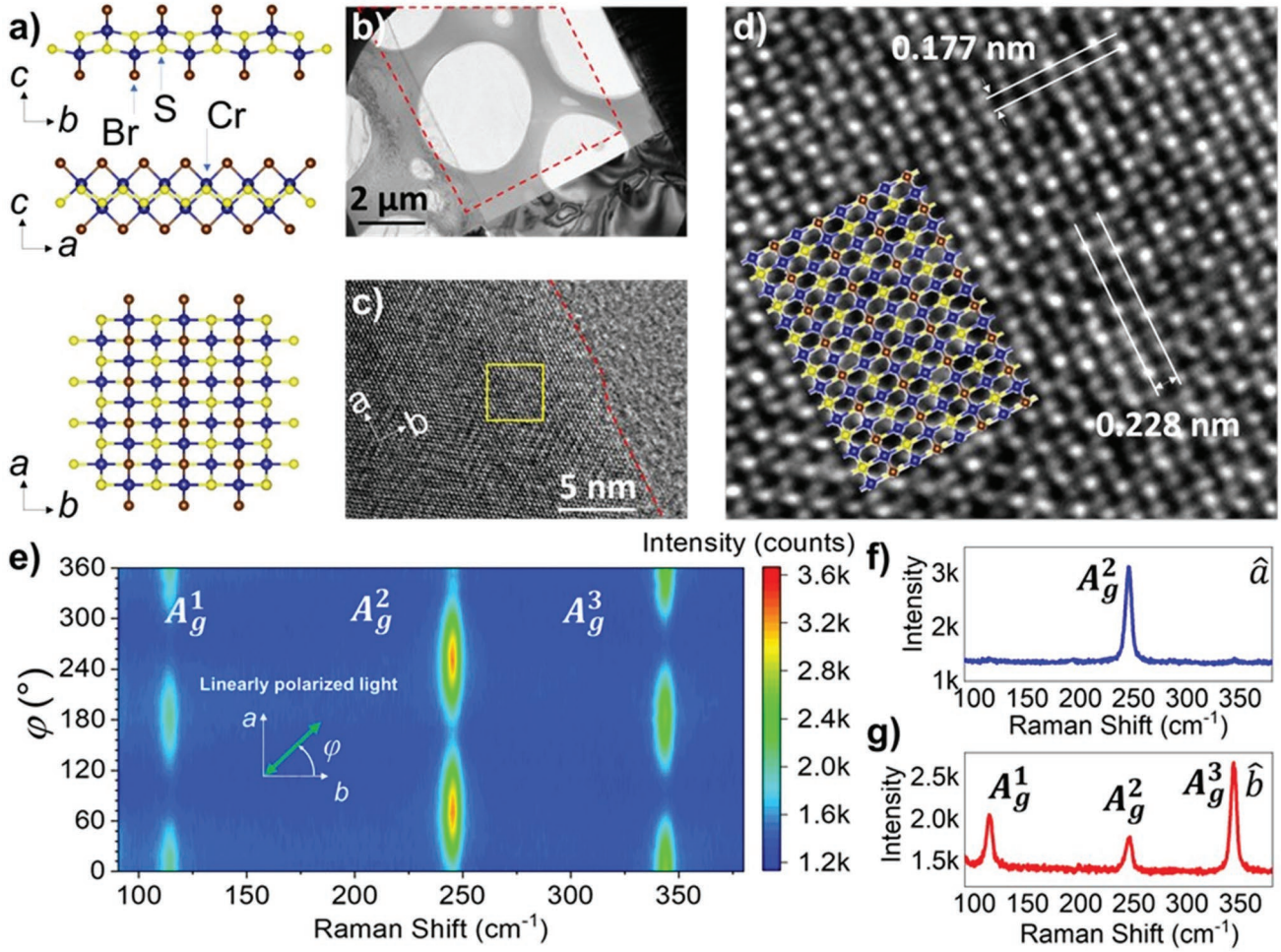

Figure 1. a) Top and side views of the crystal structure of CrSBr. b) Low magnification TEM image of the CrSBr sample, dashed red lines highlights the CrSBr thin flake area. c) Diffraction pattern of the selected area. d) High-resolution TEM image of the CrSBr flake in b). d) Zoom-in view of the selected area in c) with the simulated crystal structure overlayed for comparison. e) Polarization-dependent Raman spectra of CrSBr bulk material. The sketch in the figure shows the polarization angle φ of the linearly polarized laser relative to the crystallographic axes. f) and g) Raman spectra ($n = 3$) with the linear polarized laser excitation along *a* and *b* axes of the CrSBr crystal, respectively.

magnetic resonance field. The spectra are fitted with a Lorentzian function and the resulting magnetic resonance field, H_r and peak-to-peak linewidth, ΔH as function of θ_H and φ_H are reported in **Figure 3**.

H_r for both out-of-plane (Figure 3a) and in-plane (Figure 3b) configurations shows an oscillating behavior of the ESR signal with π periodicity, which can be fitted to the equations:[17]

$$H_r(\theta) = H_{i\perp}\cos^2\theta_H + H_{0\perp} \quad (1a)$$

$$H_r(\varphi) = H_{i\parallel}\cos^2\varphi_H + H_{0\parallel} \quad (1b)$$

where $H_{i\perp}$ and $H_{i//}$ are the perpendicular and parallel internal anisotropy fields and H_0 is the offset. From the result of the fit we obtain $H_{i\perp} = (6.7 \pm 0.1)$ mT, $H_{i//} = (1.05 \pm 0.04)$ mT, and $H_{i\perp} = (334.89 \pm 0.05)$ mT, $H_{0//} = (335.45 \pm 0.03)$ mT.

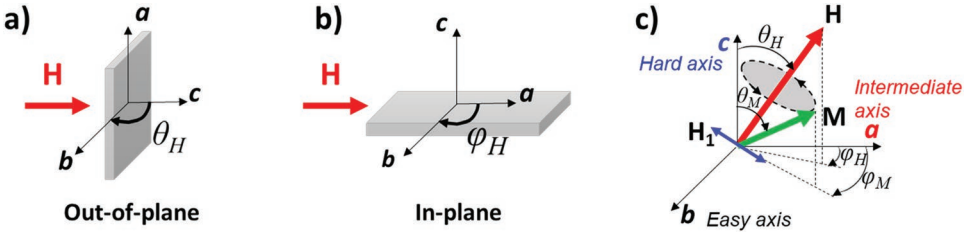

Scheme 1. Representation of the a) out-of-plane and b) in-plane configurations used for the angular dependent studies and definition of the rotation angles θ_H and φ_H. c) Precession of the magnetization vector M (green vector) around the magnetic field H (red vector) perpendicular to the microwave field H_1 (blue double arrowed line) in the ESR experiment. The magnetization absorbs the microwave energy when the precession frequency matches the frequency of the microwave photons. The crystallographic directions a, b and c and the easy, hard, and intermediate axes are shown.

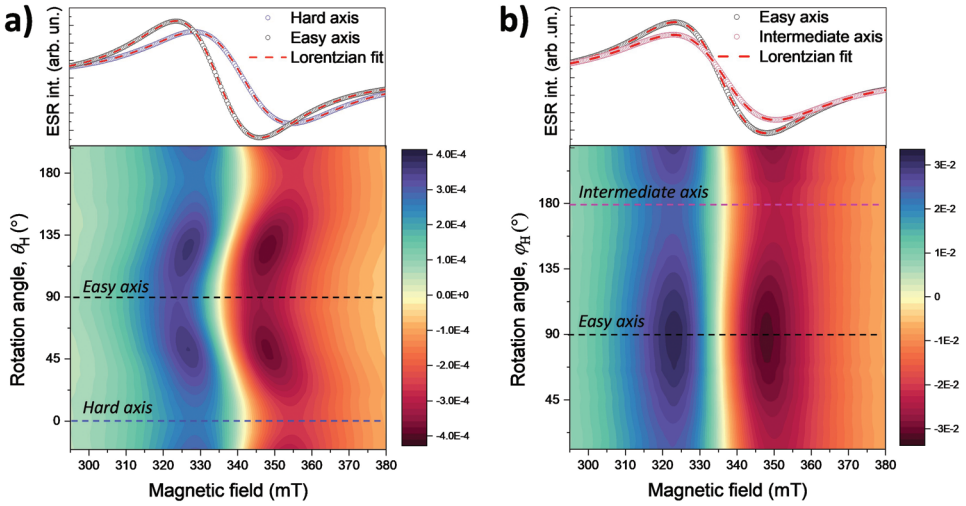

Figure 2. Contour plot of the angular dependent electron spin resonance spectra recorded at room temperature for the a) out-of-plane and b) in-plane configurations. The spectra (circles) recorded for H parallel to the hard, intermediate and easy magnetic axes are reported along with the Lorentzian simulations (solid lines) on top of the contour plots. Error bars are within the size of the dots ($n = 2$). For contour plots, spectra were recorded with 6° rotation steps.

The angular dependence of the ESR linewidth for the out-of-plane (Figure 3c) and in-plane (Figure 3d) configurations show a very different behavior. In particular, we found a *W*-like and *V*-like shape respectively which we can fit to the following equations:

$$\Delta H(\theta) = A\left(3\cos^2\theta_H - 1\right)^2 + \Delta H_{0\perp} \quad (2a)$$

$$\Delta H(\varphi) = B\left(3\cos^2\varphi_H - 1\right) + \Delta H_{0\parallel} \quad (2b)$$

where A = (2.28 ± 0.04) mT and B = (1.76 ± 0.04) mT are linewidth amplitude constants and $\Delta H_{0\perp}$ = 36 mT and $\Delta H_{0\parallel}$ = 44 mT are the offset linewidth values for the out-of-plane and in-plane configurations, respectively.

2.3. ESR Temperature Dependence

Temperature-dependent spectra recorded for H // *b* and H // *c* along with the Lorentzian fit are reported in **Figure 4**. For H // *c*, the spectra show a Lorentzian lineshape from 298 to 170 K. At lower temperatures the ESR resonance field shifts to higher fields before the signal evolves into different modes around

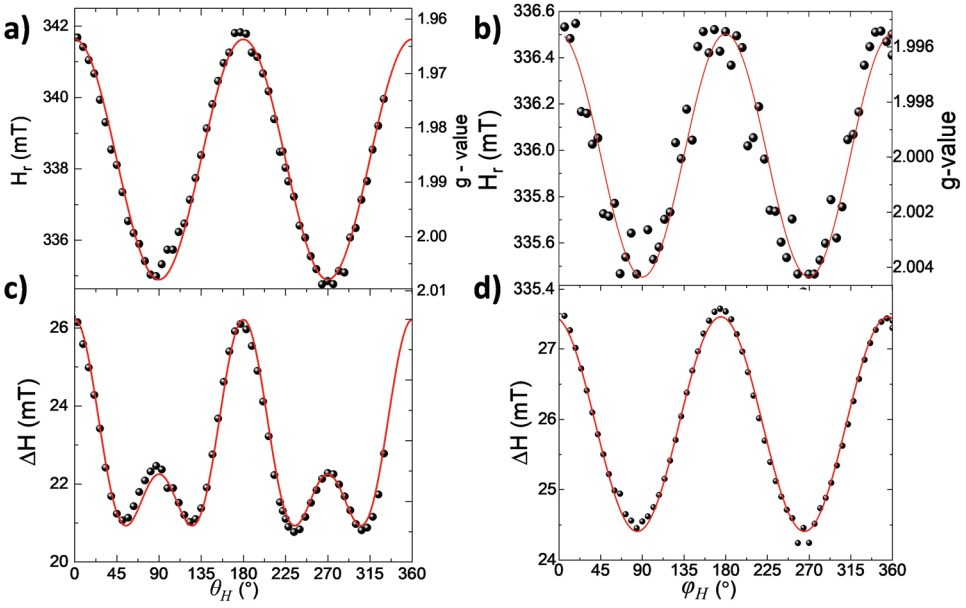

Figure 3. Angular dependence of the magnetic resonance field and peak-to-peak linewidth obtained from the fitting of the spectra in Figure 2 for the out-of-plane, a) and c) and in-plane, b) and d), configurations respectively. Circles and solid lines are the experimental data and simulations respectively. Error bars are within the size of the dots.

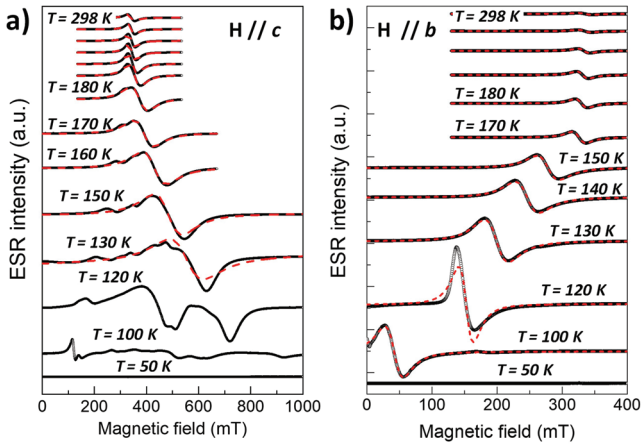

Figure 4. Temperature dependence of the electron spin resonance spectra recorded for H // *b* a) and H // *c* b). Black and red lines are the experimental spectra and simulations respectively. Error bars are within the size of the dots.

T = 150 K with resonance signals appearing across the whole magnetic field range. Consequently, the lineshape of the main peak deviates from a Lorentzian profile. The signal intensity increases from 298 to 120 K, and then decreases abruptly for T < 100 K. For H // *b* the ESR lineshape shows a Lorentzian profile from 298 K down to 130 K. Around T = 120 K the lineshape shows an anomaly with an asymmetric profile and an abrupt narrowing before restoring the Lorentzian profile at 100 K. The ESR resonance field shifts to lower fields and the signal intensity increases before becoming ESR silent for T <100 K.

In **Figure 5**a the temperature dependence of the reciprocal of the double integrated area of the ESR signal which is proportional to the imaginary component of the magnetic susceptibility (χ) is shown. For H // *c* and H // *b*, χ^{-1} follows a linear dependence for T > 200 and T > 150 K respectively while at lower temperatures it plateaus to zero. By fitting the linear dependence to the Curie-Weiss's law $\chi^{-1} = C/(T + \theta_W)$, where C is the Curie constant and θ_W the Weiss constant, we obtain $\theta_W^{\perp} \sim +180$ K and $\theta_W^{\parallel} \sim +154$ K for the H // *c* and H // *b*, respectively.

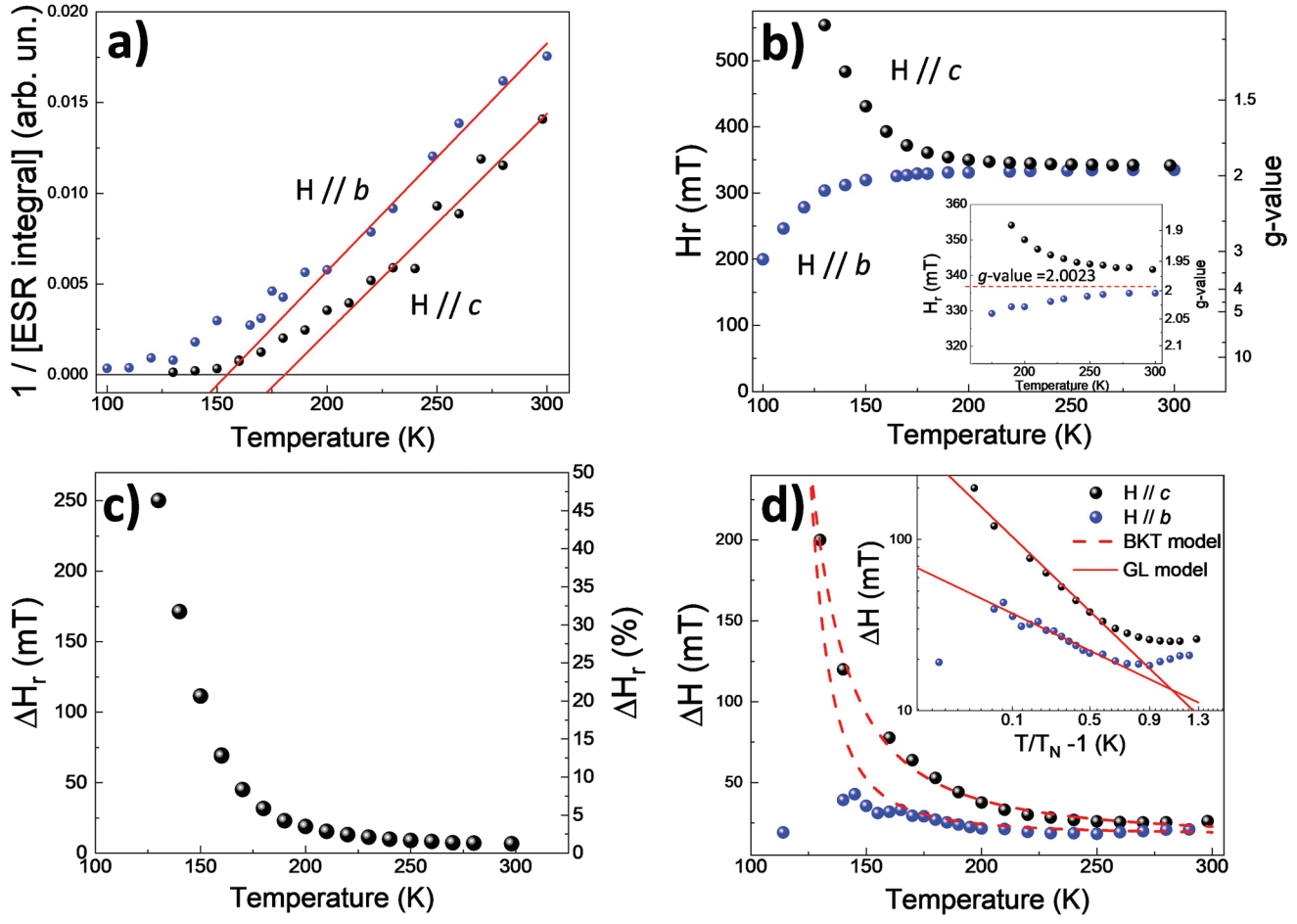

Figure 5. Temperature dependence of χ^{-1} a), H_r and *g*-value b) and ΔH_r c) and ΔH d). Lines in (a) are fit to the Curie-Weiss law (see text). Insets in (b) is a zoom of the high temperature $H_r$values. For reference, the value of the free electron *g*-value is indicated with a red dashed line. Dashed curves in d) are fitting according to the BKT model (Equation 5) and solid lines in the inset are the fitting to the logarithmic temperature dependence of ΔH according to the critical model (Equation 4). Error bars are within the size of the dots.

The temperature dependence of H_r for H // c and H // b (hereafter $H_r^{\perp}$ and $H_r^{\parallel}$) shows an opposite trend as observed in Figure 5b. At room temperature, $H_r^{\perp}$ = 341.6 mT (g_{hard}-value = 1.966) and $H_r^{\parallel}$ = 325.7 mT (g_{easy}-value = 2.005) and they both depend on the temperature by only ≈ 1% for T > 200 K. Upon approaching T_c = 180 K, $H_r^{\perp}$ and $H_r^{\parallel}$ increases and decreases respectively in a non-linear fashion from the room temperature values. Figure 5c reports the $\Delta H_r = H_r^{\parallel} - H_r^{\perp}$ and the percentage difference: $(H_r^{\parallel} - H_r^{\perp})/H_r^{\perp}$ for quantitative estimation of the temperature dependence of $H_r^{\perp}$ and $H_r^{\parallel}$ within the common temperature range. For T < 200 K the deviation is only a few percent whereas it increases quickly at lower temperatures reaching 50% at T ≈130 K.

The temperature dependence of ΔH for H // c and H //b (hereafter $\Delta H^{\perp}$ and $\Delta H^{\parallel}$) are shown in Figure 5d. At room temperature, $\Delta H^{\perp}$ = 26.2 mT and $\Delta H^{\parallel}$ = 21.3 mT. Upon cooling $\Delta H^{\perp}$ shows a weak linear decrease and then a quick increase for 100 K < T < 280 K. For T < 100 K the spectra evolve into multi resonances which make the analysis of $\Delta H^{\perp}$ complicated. For H // b, $\Delta H^{\parallel}$ can be extracted from a Lorentzian, an exception is the asymmetric spectra measured ≈ 120 K. In the temperature region 100 K – 280 K, $\Delta H^{\parallel}$ decreases linearly before going through a broad minimum centered around T = 200 K, followed by a maximum at T ≈ 150 K.

The angular dependence of H_r provides a direct determination of the magnetization axis. The direction corresponding to the lowest and highest H_r values provide the easy and hard axes of the magnetization, respectively.[18] Thus, from the fitting to Equation 1a we obtain that in the out-of-plane configuration H_r is maximum and minimum for $\theta_H \approx 0°$ (c-axis) and 90° (b-axis) which corresponds to the hard and easy axes of the magnetization, respectively (see **Scheme** 1c). In the in-plane configuration, H_r shows a relatively weak angular dependence, nevertheless we can distinguish between the lowest and highest H_r values. From the fit of the data to the Equation 1b we obtain the direction of the intermediate axis for $\varphi_H \sim 90°$, hence parallel to the a-axis.[10]

From the H_r values obtained along the easy, intermediate and hard axes directions at room temperature, we estimate the effective g-values: g_x = 1.996 ± 0.001, g_y = 2.003 ± 0.001 and g_z = 1.966 ± 0.001. The magnetic moment $\mu = g\sqrt{S(S+1)}\mu_B$ calculated along the easy, intermediate and hard axes are: 3.88, 3.86, and 3.80 μ_B respectively, which are close to the experimental magnetic moment reported for Cr^{3+} ions: μ(exp) ≈3.8 μ_B[19] with quenched orbital moment, thus confirming that the ESR signal originates from spin-only Cr^{3+} with S = 3/2.[20] Quenched orbital moment has also been reported in other Cr-based 2D magnets.[11a,21]

The generalized spin-Hamiltonian for 2D magnets reads as:

$$H = -\frac{1}{2}\sum_{i,j}\left(J\mathbf{S}_i\cdot\mathbf{S}_i + \Lambda S_i^z S_j^z\right) - \sum_i A\left(S_i^z\right)^2 \quad (3)$$

where J is the exchange coupling, Λ is the magnetic anisotropy contribution due to dipolar interaction, A is the single-ion anisotropy (i.e., magnetocrystalline anisotropy), $\mathbf{S}$ is the spin operator and i and j indicate two different sites in the lattice. Because of the quenched orbital moment, $A \sim 0$, we ascribe the magnetic anisotropy to originate mainly from magnetic dipolar interactions, $\Lambda \neq 0$ that is shape anisotropy.[22] These arguments are supported by previous studies where the significant role of shape anisotropy in CrSBr has been experimentally reported[9c,10] and theoretically predicted to be layer dependent with an even more pronounced contribution in the monolayer.[22] We stress that at temperatures well above T_C we would expect that CrSBr is purely paramagnetic. However, the dependence of the ESR signal on the orientation of the crystal relative to H at room temperature indicates the high sensitivity of the ESR technique for detection of spin–spin correlations.

In addition, due to the distortion of the Cr^{3+} octahedral environment in CrSBr, a second-order contribution from crystal field excited states of the Cr^{3+} ions could be present.[23] We note that magnetic anisotropy well above T_c is not observed in 3D materials but it is a signature of 2D magnetism. The observed W-shape in the ESR angular dependence observed for ΔH in the out of plane configuration provides an even more striking difference between a 3D and 2D magnet. The W-shape signature has been reported for other Van der Waals crystals including $Cr_2Ge_2Te_6$,[13] $CrCl_3$,[17] K_2CuF_4[24], and $MnPS_3$[25] which have experimentally shown 2D magnetic behavior.[26] Furthermore, the W-shape dependence indicates the occurrence of spin-spin correlations and long wavelength fluctuations at $q \approx 0$ of the spin wave dispersion, $\omega(q)$. Former ESR studies on 2D magnets have clearly shown that the angular dependence of ΔH transforms from a V-shape into a W-shape by cooling the crystal.[13] The fact that we observe a W-shape even at room temperature indicates the presence of a large gap in spin wave excitation spectrum, which leads to the observation of spin–spin correlations and magnetic order. Based on these considerations we conclude that the bulk CrSBr single crystal behaves like an effective 2D magnet described by the XY model.

Finally, we discuss the temperature dependence of the ESR intensity, resonance field, and linewidth. In general, the double integrated intensities of the ESR spectra at a single microwave frequency are not directly comparable to the magnetic susceptibility obtained by conventional magnetometers, because of the transition selectivity of the ESR technique. Nevertheless, from the analysis of ESR intensity, we obtain that the sign and magnitude of Weiss constant obtained for H // c agrees with previously reported Curie temperature T_c = 180 K.[8] For H // b we obtain a Weiss constant $\theta_W^{\parallel}$ significantly different from $\theta_W^{\perp}$ thus suggesting the occurrence of a second order zero-field splitting term B_2^0 responsible for the shift of the Curie temperature along the easy and hard axes.[27] B_2^0 is directly related to the difference $\theta_W^{\parallel} - \theta_W^{\perp} = \frac{3}{10}B_2^0(2J-1)(2J+1)$[28] from where we estimate B_2^0 = + 10.8 K. This value is considerably large as we might expect because of the distorted octahedral symmetry of Cr^{3+} ions within the lattice and it has a positive sign, further corroborating that the easy axis lies in the plane of the crystal. We note that the ESR signal disappears below 100 K for both orientations H // c and H // b. This behavior is clearly in contrast to what has been reported for ESR studies of 2D ferromagnets such as CrBr3,[11a] $CrCl_3$,[13] $Cr_2Ge_2Te_6$.[15b] Instead it agrees with other Cr-based 2D antiferromagnets[11c], thus corroborating the observation of AF order in CrSBr where the AF coupling between the layers leads to a vanishing ESR signal.

The resonance field deviation from the room temperature values in opposite directions for H // c and H // b is ascribed to

the increased magnetic anisotropy which tends to pin the CrSBr magnetization along the easy axis with the decrease of thermal fluctuations. It also shows the presence of the weak magnetic anisotropy at room temperature due to dipolar interactions which make the CrSBr crystal to deviate from an ideal paramagnet.

The temperature dependence of ΔH reported in Figure 5d shows a striking difference between $\Delta H_r^{\perp}$ and $\Delta H_r^{\parallel}$ The former increases quickly below 200 K and develops into multi-resonance modes which make cumbersome the extraction of a peak-to peak linewidth. For H // *b*, the ESR spectra lineshape preserves a Lorentzian lineshape for the whole temperature range which makes $\Delta H^{\perp}$ observable through T_N except for $T = 120$ K and before the signal disappear for $T < 100$ K.

In strongly interacting systems the linewidth scales as $\frac{\omega_{dip}^2}{\omega_{exc}}$, where $\omega_{dip}$and ω_{exc} are the dipolar and exchange interaction frequencies: it broadens quickly for dipolar magnetic interactions and narrows in the temperature regime where the magnetic exchange interactions dominate. The latter phenomena is called *exchange narrowing*. Thus, in the temperature region above T_c we expect that the linewidth increases upon cooling, whereas as observed for H // *b*, $\Delta H^{\parallel}$ reaches a maximum and then decreases by approaching T_N, because of the onset of AF exchange interactions between the van der Waals layers.

By plotting $\Delta H(T)/\Delta H(\infty)$ versus $(T–T_N)/T_N$ (not shown) we observe that for H // *c* and H // *b* the region with large linewidths extend for $(T–T_N)/T_N < 0.9$ and 0.5 respectively. This result agrees with the observation that $\Delta H(T)/\Delta H(\infty)$ for 2D magnets extends to a wider $(T–T_N)/T_N$ region compared to the 3D magnets[12b].

Because $(T–T_N)/T_N$ <0.1 for both orientations, we can model the temperature dependence of ΔH, Figure 5c, according to the Ginzburg-Landau critical model for the ESR linewidth:

$$\Delta \mathrm{H(T)} = \frac{\mathrm{Q}}{\left(\frac{\mathrm{T}}{\mathrm{T_N}} - 1\right)^{\mathrm{p}}} \tag{4}$$

where *Q* is a constant and *p* is critical exponent which depends on the dimensionality of the system. In the inset of Figure 5d, is reported the logarithmic plot of $\Delta H(T)$ where the monotonously increasing linear dependence within the temperature region 150 K < *T* < 250 K is fitted with the linearized form of the Equation 4 with critical exponent $p = 3.4$ and 1.7 for H // *c* and H // *b* respectively which are in the range of those previously reported for other layered AF systems.[26]

The in-plane easy axis, the *W*-shape angular dependence of ΔH as well as the spin-spin correlations and the temperature dependence of ΔH, altogether point out to a 2D XY magnet. Thus, CrSBr might provide a model system for the observation of topological phase transitions and of the formation of bound vortex and antivortex pairs below the transition temperature T_{BKT}. As shown by Hemmida et al.[11c], $\Delta H \propto \xi^3$ where ξ is spin correlation length within the BKT: $\xi(T)^{-1} = \left(\frac{T}{T_{BKT}} - 1\right)$ with $\nu = 1/2$ for the XY model. Thus:

$$\Delta \mathrm{H(T)} = \Delta \mathrm{H_\infty} \exp\left(\frac{3\mathrm{b}}{\sqrt{\frac{\mathrm{T}}{\mathrm{T_{BKT}}} - 1}}\right) + mT + \Delta \mathrm{H_0} \tag{5}$$

The fitting of ΔH to the Equation 5 provides T_{BKT} = (76 ± 2) K and (92 ± 10) K for H // *c* and H // *b*, respectively which are significantly lower than T_N. This might indicate a scenario where AF order and spin fluctuations exist in the temperature region $T_{BKT} < T < T_N$ as suggested for other Cr-based 2D magnets.[11c]

3. Conclusions

We have reported on the angular and temperature ESR properties of a bulk CrSBr single crystal. Remarkably, the formal CrSBr single crystal reveals XY antiferromagnetism as inferred from the in-plane easy axis, the *W*-shape angular dependence of ΔH and the spin–spin correlations at temperature well above the Néel temperature. We also estimate the zero-field splitting parameter and ascribe the magnetic anisotropy originating from magnetic dipolar interactions with partial contribution from excited crystal field states because of the quenched orbital magnetic moment and distorted octahedral environment of Cr^{3+} ions. We validate the critical model and analyze our results within the BKT model suggesting the occurrence of vortex and antivortex pairs coexisting with antiferromagnetic order at relatively high temperatures. Overall, our approach enables the investigation of spin-spin correlation lengths in CrSBr which could be extended to other VdW layered magnets. These findings together with the previously assessed magneto-transport properties and chemical stability of CrSBr demonstrate that CrSBr is a promising layered magnet for future magneto- and topological-electronics. Future work will be devoted to the investigation of topological transitions in the monolayer limit. We envisage that by exploiting the magneto-transport properties of CrSBr and the high sensitivity of the electrically detected magnetic resonance (EDMR) technique it will be possible to study the layer-dependent magnetic resonance properties down to the monolayer that could potentially lead to the observation of new functional magnetic properties.

4. Experimental Section

Bulk Crystal Synthesis: The single crystal of CrSBr was synthesized by a chemical vapor transport method. Chromium, sulfur, and bromine with 1:1:1 were added and sealed in a quartz tube under high vacuum, and then put into a two-zone tube furnaces. After 10 h of pre-reaction at 700 °C, the source and growth ends were kept at 850 and 900 °C, respectively. After 25 h, the temperature gradient was reversed, and the hot end gradually increased from 880 to 950 °C in 5 days period. The high-quality CrSBr single crystals with lengths up to 2.5 cm were collected from the cold end of the tube.

High-Resolution Scanning Transmission Electron Microscopy: The CrSBr samples for STEM study were prepared by using a wet transfer technique. The CrSBr thin flakes were prepared onto SiO_2/Si wafer by using mechanical exfoliation. Then the substrate was spin-coated with PMMA at 4000 rpm for 1 min. By using 10% NaOH solution, the PMMA film with CrSBr samples attached on the backside was separated from the Si wafer and floated on the surface. Lacey carbon TEM grids were used to pick up the PMMA film. After the PMMA was removed by acetone, TEM grid with CrSBr flakes was prepared for further measurements. The morphology and crystal structure of CrSBr thin flakes were investigated by using ZEISS-SUPRA55 and Tecnai-F20.

X-Ray Photoelectron Spectroscopy: X-Ray photoelectron spectroscopy (XPS) was conducted on a Thermo ScientificTM K-AlphaTM+ spectrometer equipped with a monochromatic Al Kα X-ray source (1486.6 eV) operating at 100 W. Samples were analyzed under vacuum ($P < 10^{-8}$ mbar) with a pass energy of 150 eV (survey scans) or 25 eV (high-resolution scans). All peaks would be calibrated with C1s peak binding energy at 284.8 eV for adventitious carbon.

Raman Spectroscopy: The micro-Raman spectroscopy was investigated by using a Raman system (FST2-Ahdx-DZ, Zolix) equipped with a monochromator. 532 nm solid state laser was used as the excitation source, whose linear polarization can be changed by adding a $\lambda/2$ wave plate. A long working distance 50x objective lens was used to acquire data. The 1800 grooves mm^{-1} grating was chosen for the spectra measurements.

Electron Spin Resonance: The ESR spectra were recorded with a Varian E15 spectrometer and a Bruker super high Q cavity operated at X-band. The static magnetic field was modulated at 100 kHz with modulation amplitude of 4 Gauss. The magnetic field was monitored continuously with a Hall probe. Sample temperatures in the range 4–300 K were obtained with an Oxford ESR 900 cryostat. The single crystal was mounted on a suprasil quartz rod and into a goniometer with ½ degree sensitivity for crystal rotation measurements. A DPPH sample was used as reference to determine the *g*-factors and a N-doped diamond sample was used for calibration of the crystal direction relative to the magnetic field vector. All the ESR spectra were fitted with an implemented MatLab routine to the first derivative of a Lorentzian function: $y = \Gamma\left(\frac{H-H_r}{\Delta H^3}\right)\left(1+\frac{4}{3}\frac{(H-H_r)}{\Delta H^2}\right)^{-2}$ where Γ is the ESR amplitude. Peak-to-peak linewidths ΔH are related to the full-width half maximum $\Delta H_{1/2}$ obtained from the Lorentzian fit with the relation: $\Delta H = \Delta H_{1/2}/\sqrt{3}$. OriginPro 2021 version 9.8.0.200 was used for fittings of the data in Figure 5a,d and were performed with a Levenberg–Marquardt itineration algorithm.

Supporting Information

Supporting Information is available from the Wiley Online Library or from the author.

Acknowledgements

X.L. gratefully acknowledges financial support from the National Science Foundation of China (Grant No. 12104006), and the Center of Strong Laser and High Magnetic Field at Anhui University. L.L. was partly supported by the Pioneer Hundred Talents Program of the Chinese Academy of Sciences (E24BHD17). Z.S. was supported by Czech Science Foundation (GACR No. 20–16124J). A.S. received funding from the European Union's Horizon 2020 research and innovation programme (Grant No. 956813). The University of Milano-Bicocca for open access funding through the CRUI-CARE agreement.

Open Access Funding provided by Universita degli Studi di Milano-Bicocca within the CRUI-CARE Agreement.

Conflict of Interest

The authors declare no conflict of interest.

Data Availability Statement

The data that support the findings of this study are openly available in board.unimib.it at https://doi.org/10.17632/v73n4nnd2v.1, reference number 1.

Keywords

2D magnets, BKT transition, CrSBr, electron spin resonance, magnetic anisotropy

Received: June 21, 2022
Revised: July 27, 2022
Published online:

[1] R. D. T. Araujo, J. Zarpellon, D. H. Mosca, *J. Phys. D: Appl. Phys.* **2022**, *55*, 283003.
[2] Z. Jiang, P. Wang, J. P. Xing, X. Jiang, J. J. Zhao, *ACS Appl. Mater. Interfaces* **2018**, *10*, 39032.
[3] C. Gong, L. Li, Z. L. Li, H. W. Ji, A. Stern, Y. Xia, T. Cao, W. Bao, C. Z. Wang, Y. A. Wang, Z. Q. Qiu, R. J. Cava, S. G. Louie, J. Xia, X. Zhang, *Nature* **2017**, *546*, 265.
[4] S. B. Chen, C. X. Huang, H. S. Sun, J. F. Ding, P. Jena, E. J. Kan, *J. Phys. Chem. C* **2019**, *123*, 17987.
[5] N. D. Mermin, H. Wagner, *Phys. Rev. Lett.* **1966**, *17*, 1133.
[6] J. M. Kosterlitz, D. J. Thouless, *J. Phys. C: Solid State Phys.* **1973**, *6*, 1181.
[7] a) H. Wang, J. S. Qi, X. F. Qian, *Appl. Phys. Lett.* **2020**, *117*, 052403; b) M. Gibertini, M. Koperski, A. F. Morpurgo, K. S. Novoselov, *Nat. Nanotechnol.* **2019**, *14*, 408.
[8] a) K. Lee, A. H. Dismukes, E. J. Telford, R. A. Wiscons, J. Wang, X. D. Xu, C. Nuckolls, C. R. Dean, X. Roy, X. Y. Zhu, *Nano Lett.* **2021**, *21*, 3511; b) E. J. Telford, A. H. Dismukes, K. Lee, M. H. Cheng, A. Wieteska, A. K. Bartholomew, Y. S. Chen, X. D. Xu, A. N. Pasupathy, X. Y. Zhu, C. R. Dean, X. Roy, *Adv. Mater.* **2020**, *3*, 2003240.
[9] a) Y. Guo, Y. H. Zhang, S. J. Yuan, B. Wang, J. L. Wang, *Nanoscale* **2018**, *10*, 18036; b) C. Ye, C. Wang, Q. Wu, S. Liu, J. Zhou, G. Wang, A. Söll, Z. Sofer, M. Yue, X. Liu, M. Tian, Q. Xiong, W. Ji, X. Renshaw Wang, *ACS Nano* **2022**, *16*, 11876; c) E. J. Telford, A. H. Dismukes, R. L. Dudley, R. A. Wiscons, K. Lee, D. G. Chica, M. E. Ziebel, M. G. Han, J. Yu, S. Shabani, A. Scheie, K. Watanabe, T. Taniguchi, D. Xiao, Y. M. Zhu, A. N. Pasupathy, C. Nuckolls, X. Y. Zhu, C. R. Dean, X. Roy, *Nat. Mater.* **2022**, *21*, 754; d) F. Wu, I. Gutierrez-Lezama, S. A. Lopez-Paz, M. Gibertini, K. Watanabe, T. Taniguchi, F. O. von Rohr, N. Ubrig, A. F. Morpurgo, *Adv. Mater.* **2022**, *34*, 2109759.
[10] O. Goser, W. Paul, H. G. Kahle, *J. Magn. Magn. Mater.* **1990**, *92*, 129.
[11] a) C. L. Saiz, J. A. Delgado, J. van Tol, T. Tartaglia, F. Tafti, S. R. Singamaneni, *J. Appl. Phys.* **2021**, *129*, 233902; b) A. Ashoka, K. S. Bhagyashree, S. V. Bhat, *Phys. Rev. B* **2020**, *102*, 024429; c) M. Hemmida, H. A. K. von Nidda, V. Tsurkan, A. Loidl, *Phys. Rev. B* **2017**, *95*, 224101.
[12] a) R. J. Birgeneau, H. J. Guggenheim, G. Shirane, *Phys. Rev. B* **1973**, *8*, 304; b) H. W. Dewijn, L. R. Walker, H. J. Guggenhe, J. L. Davis, *Solid State Commun.* **1972**, *11*, 803; c) C. Pich, F. Schwabl, *Phys. Rev. B* **1994**, *49*, 413; d) Y. Yokozawa, *J. Phys. Soc. Jpn.* **1971**, *31*, 1590.
[13] J. Zeisner, K. Mehlawat, A. Alfonsov, M. Roslova, T. Doert, A. Isaeva, B. Buchner, V. Kataev, *Phys. Rev. Mater.* **2020**, *4*, 064406.
[14] Y. C. Xun, Z. Y. Zhu, X. F. Chen, J. S. Qi, *Phys. Rev. B* **2021**, *104*, 085429.
[15] a) T. Sakurai, B. Rubrecht, L. T. Corredor, R. Takehara, M. Yasutani, J. Zeisner, A. Alfonsov, S. Selter, S. Aswartham, A. U. B. Wolter, B. Buchner, H. Ohta, V. Kataev, *Phys. Rev. B* **2021**, *103*, 024404; b) J. Zeisner, A. Alfonsov, S. Selter, S. Aswartham, M. P. Ghimire, M. Richter, J. van den Brink, B. Buchner, V. Kataev, *Phys. Rev. B* **2019**, *99*, 165109.
[16] arXiv:2205.13456.
[17] S. Chehab, J. Amiell, P. Biensan, S. Flandrois, *Physica B* **1991**, *173*, 211.

[18] M. Farle, *Rep. Prog. Phys.* **1998**, *61*, 755.
[19] C. Kittel, *Introduction to Solid State Physics*, Weily, New York **1996**.
[20] A. Abragam, B. Bleaney, *Electron Paramagnetic Resonance of Transition Ions*, Oxford University Press, Oxford **1970**.
[21] a) M. Hemmida, H. A. K. von Nidda, N. Buttgen, A. Loidl, L. K. Alexander, R. Nath, A. V. Mahajan, R. F. Berger, R. J. Cava, Y. Singh, D. C. Johnston, *Phys. Rev. B* **2009**, *80*, 054406; b) M. Hemmida, H.-A. Krug von Nidda, A. Loidl, *J. Phys. Soc. Jpn.* **2011**, *80*, 053707.
[22] K. Yang, G. Y. Wang, L. Liu, D. Lu, H. Wu, *Phys. Rev. B* **2021**, *104*, A25.
[23] J. L. Lado, J. Fernandez-Rossier, 2d Maters **2017**, *4*, 035002.
[24] I. Yamada, I. Morishita, T. Tokuyama, *Physica B & C* **1983**, *115*, 179.
[25] K. Okuda, K. Kurosawa, S. Saito, M. Honda, Z. Yu, M. Date, *J. Phys. Soc. Jpn.* **1986**, *55*, 4456.
[26] L. J. D. Jongh, *Magnetic Properties of Layered Transition Metal Compounds*, Springer, Dordrecht, **1990**.
[27] Y. L. Wang, *Phys. Lett. A* **1971**, *35*, 383.
[28] M. O. Ajeesh, T. Shang, W. B. Jiang, W. Xie, R. D. dos Reis, M. Smidman, C. Geibel, H. Q. Yuan, M. Nicklas, *Sci. Rep.* **2017**, *7*, 7338.